The Meteoritical Society

Meteoritics & Planetary Science 45, Nr 12, 1929–1947 (2011)
doi: 10.1111/j.1945-5100.2010.01131.x

Petrogenesis of lunar meteorite Northwest Africa 2977: Constraints from in situ microprobe results

Ai-Cheng ZHANG[1,2,3*], Wei-Biao HSU[2,4], Christine FLOSS[5], Xian-Hua LI[6], Qiu-Li LI[6], Yang LIU[3], and Lawrence A. TAYLOR[3]

[1]State Key Laboratory for Mineral Deposits Research, School of Earth Sciences and Engineering, Nanjing University, Nanjing 210093, China
[2]Laboratory for Astrochemistry and Planetary Sciences, Purple Mountain Observatory, Nanjing 210008, China
[3]Department of Earth and Planetary Sciences, Planetary Geosciences Institute, University of Tennessee, Knoxville, Tennessee 37996, USA
[4]Faculty of Earth Sciences, China University of Geosciences, Wuhan 430074, China
[5]Laboratory for Space Sciences and Physics Department, Washington University, Saint Louis, Missouri 63130, USA
[6]State Key Laboratory of Lithospheric Evolution, Institute of Geology and Geophysics, Chinese Academy of Sciences, Beijing 100029, China
[*]Corresponding author. E-mail: zhangach@hotmail.com

(Received 26 April 2010; revision accepted 28 August 2010)

Abstract–Northwest Africa (NWA) 2977 is an olivine-gabbro lunar meteorite that has a distinctly different petrographic texture from other lunar basalts. We studied this rock with a series of in situ analytical methods. NWA 2977 consists mainly of olivine and pyroxene with minor plagioclase. It shows evidence of intense shock metamorphism, locally as high as shock-stage S6. Olivine adjacent to a melt vein has been partially transformed into ringwoodite and Al,Ti-rich chromite grains have partially transformed into their high-pressure polymorph (possibly $CaTi_2O_4$-structure). Olivine in NWA 2977 contains two types of lithic inclusions. One type is present as Si,Al-rich melt inclusions that are composed of glass and, in most cases, dendritic pyroxene. The other type is mafic and composed of relatively coarse-grained augite with accessory chromite, RE-merrillite, and baddeleyite. Two Si,Al-rich melt inclusions are heavy rare earth elements (REE) enriched, whereas the mafic inclusion has high REE concentrations and a KREEP-like pattern. The mafic inclusion could be a relict fragment captured during the ascent of the parent magma of NWA 2977, whereas the Si,Al-rich inclusions may represent the original NWA 2977 melt. The calculated whole-rock composition has a KREEP-like REE pattern, suggesting that NWA 2977 has an affinity to KREEP rocks. Baddeleyite has recorded a young crystallization age of 3123 ± 7 Ma (2σ), which is consistent with results from previous whole-rock and mineral Sm-Nd and Rb-Sr studies. The petrography, mineralogy, trace element geochemistry, and young crystallization age of NWA 2977 support the possibility of pairing between NWA 2977 and the olivine-gabbro portion of NWA 773.

INTRODUCTION

Apollo and Luna samples have provided a fundamental understanding of the origin and evolution of the Moon (e.g., Warren 1985; Papike et al. 1998; Jolliff et al. 2006). However, they were collected from a relatively small (5–8%) and geochemically anomalous region of the Moon's surface (Warren and Kallemeyn 1991), limiting our understanding of the global Moon. However, in addition to the returned materials, approximately 65 (including paired) lunar meteorites have been identified in the past three decades from Antarctica and hot-desert collections (e.g., Oman and Northwest Africa; Korotev 2005; Korotev et al. 2009). These objects come from craters that are randomly distributed on the lunar surface, including possibly from

the lunar farside (e.g., Takeda et al. 2006; Hsu et al. 2008; Korotev et al. 2009), and provide a complementary data source for our understanding of the nature and internal evolution of the Moon (e.g., Korotev et al. 2003, 2009; Korotev 2005; Terada et al. 2007). Ten of these lunar meteorites are unbrecciated basalts (Asuka-881757, LaPaz Icefield 02205/02224/02226/02436/03632/04841, Miller Range 05035, Northwest Africa [NWA] 032/479, NWA 4734, NWA 4898, and Yamato-793169) or breccias containing large clasts (>90%) of unbrecciated basalt (Dhofar 287, Northeast Africa [NEA] 003, and NWA 773 clan). Among them, the NWA 773 clan is characterized by a high abundance of olivine (Fagan et al. 2003; Jolliff et al. 2003), distinctly different from other lunar basalts and highland gabbroic rocks.

The NWA 773 clan of lunar meteorites includes NWA 773, NWA 2700, NWA 2727, NWA 2977, NWA 3160, and NWA 3333. Assuming that these stones are source-crater paired, the original lunar meteorite consisted of fragmental and regolith breccias with large clasts of olivine-phyric basalt and petrogenetically related olivine gabbro (Jolliff et al. 2007). In this clan, NWA 2977 contains only olivine gabbro. Brief results of the petrography, mineralogy (Bunch et al. 2006), bulk geochemistry (Zeigler et al. 2007), ^{40}Ar-^{39}Ar age (Burgess et al. 2007), and Sm-Nd and Rb-Sr ages (Nyquist et al. 2009) of NWA 2977 have been reported as conference abstracts. Burgess et al. (2007) reported a young ^{40}Ar-^{39}Ar age of 2.77 ± 0.04 Ga, which is in agreement with the ^{40}Ar-^{39}Ar age (2.67 ± 0.04 Ga) of similar clasts in NWA 773 (Fernandes et al. 2003). This agreement supports the suggestion that NWA 2977 and NWA 773 could be paired. Recent investigation (Nyquist et al. 2009) of the Sm-Nd and Rb-Sr systems of NWA 2977 reported ages of 3.10 ± 0.05 and 3.29 ± 0.11 Ga, respectively, older than the ^{40}Ar-^{39}Ar age and slightly older than the revised Sm-Nd age of NWA 773 (2.993 ± 0.033 Ga; Borg et al. 2009). To further understand the petrogenetic history of this meteorite, we performed a series of in situ studies on NWA 2977. Preliminary results were reported by Zhang and Hsu (2008) and Zhang et al. (2010a).

In lunar rocks and meteorites, baddeleyite is an important late-stage, U-bearing mineral that has been used to determine the crystallization ages of lunar rocks and meteorites (e.g., Rasmussen et al. 2008; Zhang et al. 2010b). Compared to silicate minerals used for Rb-Sr, Sm-Nd, and Ar/Ar dating, baddeleyite is less susceptible to shock metamorphism (e.g., Niihara et al. 2009); thus, considering the pervasive complex impact events on the surface of the Moon, baddeleyite could record an age closer to the true crystallization age of rocks than do silicate minerals (e.g., Zhang et al. 2010b). To obtain a reliable crystallization age, the baddeleyite Pb/Pb age of NWA 2977 was determined by secondary ion mass spectrometry (SIMS).

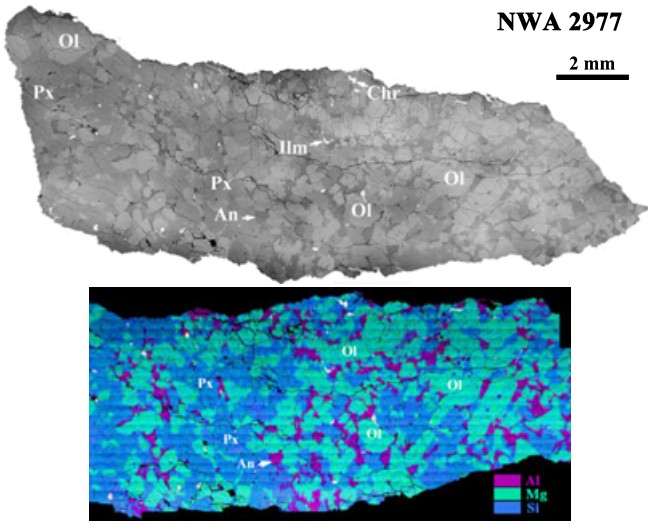

Fig. 1. Backscattered electron (BSE) image (a) and combined elemental X-ray maps (b) of Al, Mg, and Si superimposed on a BSE image of NWA 2977. Ol, olivine; Px, pyroxene; An, anorthite; Chr, chromite; Ilm, ilmenite.

ANALYTICAL METHODS

Petrography and Mineralogy

A slice of NWA 2977 was acquired from Michael Farmer, the holder of the main mass of this meteorite. One polished section was prepared from this slice. The petrography of NWA 2977 was studied using an optical microscope and a Hitachi S-3400N II scanning electron microscope (SEM), in backscattered electron (BSE) imaging mode. Modal abundances of minerals were estimated by combining elemental X-ray mapping images with BSE images (Fig. 1).

Mineral chemistry was analyzed with a JEOL 8100 electron microprobe (EMP) at Nanjing University and a Cameca SX-100 EMP at the University of Tennessee. The operating conditions were 15–20 kV accelerating voltage, 10 nA beam current for feldspar and 20 nA beam current for other minerals, and a 2–5 μm defocused beam for plagioclase and K-feldspar and a focused beam for other minerals. Melt inclusions in olivine were analyzed with a defocused beam of 5–15 μm. Four to five analyses were performed on each melt inclusion. Natural and synthetic samples were used as standards. Typical detection limits for the oxides of most elements are 0.03 wt%. Data were reduced by ZAF and PAP procedures, for JEOL and Cameca probes, respectively.

Renishaw (RM2000 and inVia Plus) microRaman spectrometers with a CCD detector at Nanjing University and the National Center for Nanoscience and

Technology of China, respectively, were used to identify minerals. The operating conditions on the RM2000 spectrometer were the same as reported by Zhang et al. (2006). The excitation laser wavelength was 514 nm, and the laser energy was 5 mW for silicate minerals and 2 mW for chromite. Raman spectra of olivine, Al,Ti-rich chromite, and their high-pressure polymorphs were obtained using the InVia Plus Raman spectrometer. The excitation laser wavelength was 785 nm, and the laser energy was 10 mW (2 mW for chromite).

Trace Element Analysis

Concentrations of rare earth elements (REE) and other trace elements in minerals were measured at Washington University, St. Louis with the modified Cameca IMS-3f ion microprobe following the procedures of Floss (2000) and Floss et al. (2008). We used an O^- primary beam of 1–5 nA (resulting in spot sizes of 10–30 μm) and energy filtering at low mass resolution to remove complex molecular interferences. The resulting mass spectrum was deconvolved in the mass ranges K-Ca-Sc-Ti, Rb-Sr-Y-Zr, and Ba-REE to remove simple molecular interferences that are not eliminated with energy filtering (Alexander 1994; Hsu 1995). Sensitivity factors for the REE in pyroxene and Ca-phosphate are from Zinner and Crozaz (1986) and for plagioclase are from Floss and Jolliff (1998). Sensitivity factors for other elements in plagioclase and pyroxene are from Hsu (1995) and are from Table 1 of Floss et al. (1998). Absolute concentrations are determined using sensitivity factors relative to Si for the silicates and Ca for the phosphates. Twenty-eight ion microprobe, trace element analyses were performed on different minerals. REE abundances in the figures are normalized to the CI chondrite abundances of Anders and Grevesse (1989).

Baddeleyite Pb/Pb Dating

Baddeleyite Pb/Pb dating was conducted by using the CAMECA IMS-1280 ion microprobe at the Institute of Geology and Geophysics of Chinese Academy of Sciences following the procedures of Li et al. (2009) and Zhang et al. (2010b). The O_2^- primary ion beam was accelerated at −13 kV, with an intensity of approximately 100 pA. To obtain a small beam size, a Gaussian illumination mode was used, and the ellipsoidal spot is about 5 μm in size. Positive secondary ions were extracted with a 10 kV potential. Oxygen flooding was used to increase the O_2 pressure to approximately 5×10^{-6} torr in the sample chamber to enhance Pb^+ sensitivity (Li et al. 2009, 2010). Four electron multipliers were used to measure simultaneously secondary ion beam intensities of ^{204}Pb, ^{206}Pb, ^{207}Pb, and $^{90}Zr_2{}^{16}O_2$ with an integration time of 6 s. The $^{90}Zr_2{}^{16}O_2$ was monitored to ensure that the measurements were on baddeleyite rather than other phases. Each measurement consisted of 150 cycles. A nuclear magnetic resonance controller was used to stabilize the magnetic field. The mass resolution was 8000 and the relative yield of each electron multiplier was calibrated using a Phalaborwa baddeleyite standard (Heaman 2009). Before measuring secondary ions, an area of 20 × 20 μm was rastered with a 2 nA primary ion beam to remove possible contaminants. Correction of common Pb was made by measuring ^{204}Pb and using a common lead composition of $^{206}Pb/^{204}Pb = 18 \pm 2$ and $^{207}Pb/^{206}Pb = 0.858 \pm 0.2$ (cf. Nemchin et al. 2009). External errors were considered when calculating the errors of corrected $^{207}Pb/^{206}Pb$ ratios in the baddeleyite. Note, however, that U-Pb system concordance cannot be checked, because U isotopes were not measured in this study.

Table 1. Modal mineralogy (vol%) of Northwest Africa (NWA) 2977 and olivine-gabbro cumulate in NWA 773.

	NWA 2977		Olivine-gabbro cumulate in NWA 773	
	This study	Bunch et al.	Fagan et al.	Jolliff et al.
Olivine	41.1	51	55.5	48
Low-Ca pyroxene	39.1	23	18.9	29
Augite	11.9	9	8.7	11
Plagioclase	7.1	14	14.2	11
Oxide phases	0.5		1.2	tr
Phosphate	0.2			tr
K-feldspar	0.1		1.6	tr

Note: tr = trace amount.

RESULTS

Petrography and Mineralogy

Northwest Africa 2977 is mainly composed of olivine and pyroxene with minor plagioclase. In hand specimen, fresh surfaces of NWA 2977 appear light green because of the high abundance of coarse-grained olivine. Olivine grains form a cumulate texture with interstices filled by irregular pyroxene grains, or occur within poikilitic pyroxene grains (Fig. 1). Plagioclase occurs as irregular interstitial crystals between olivine and pyroxene. Accessory minerals include chromite, ilmenite, phosphate, baddeleyite, K-feldspar, troilite, and Fe-Ni metal. The modal abundances of minerals in our section are given in Table 1. Our sample has less

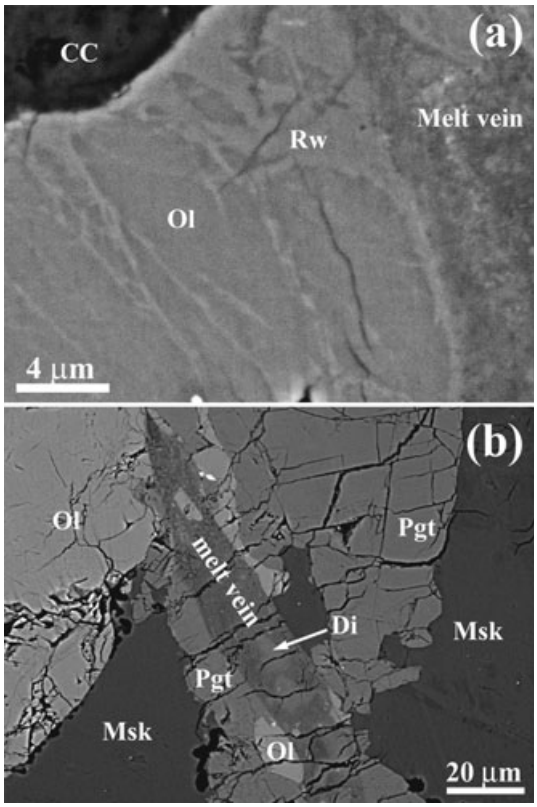

Fig. 2. Backscattered electron images of shock-induced melt veins in NWA 2977. a) Adjacent to a melt vein, olivine (Ol) has partially transformed into ringwoodite (Rw). A calcium carbonate (CC) deposit occurs in the fracture. b) Relict fragments of olivine and diopside (Di) are included in the melt vein. The melt vein cuts grains of olivine, pigeonite (Pgt), and maskelynite (Msk).

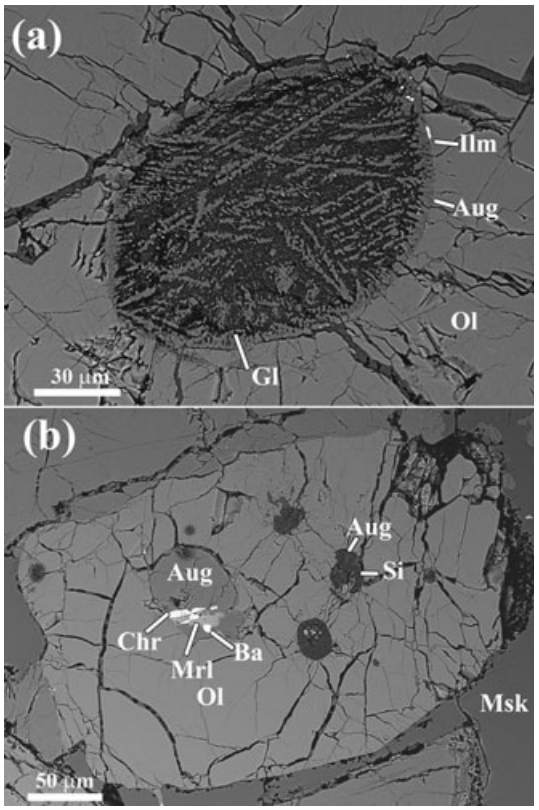

Fig. 3. Backscattered electron images of melt inclusions in olivine. a) A melt inclusion composed of fine-grained augite (Aug) and ilmenite (Ilm) set in glass (Gl). b) An olivine (Ol) grain containing Si,Al-rich inclusions and also a mafic inclusion. The Si,Al-rich inclusions consist of silica (Si) and augite (Aug). The mafic inclusion consists of augite, Al,Ti-rich chromite (Chr), merrillite (Mrl), and baddeleyite (Ba).

olivine and plagioclase and more pyroxene than another sample of NWA 2977 (Bunch et al. 2006) and than olivine-gabbro clasts in NWA 773 (Fagan et al. 2003; Jolliff et al. 2003). The apparent difference in modal abundance is probably due to the coarse-grain size of this small sample, and reflects the heterogeneous distribution of its constituent minerals. A few thin shock-induced melt veins (<20 μm in width) and melt pockets are observed in the section (Fig. 2). Weathering consists of calcite occurs on the surface and along fractures in the sample.

Olivine and Melt Inclusions

Olivine mainly occurs as equant and subhedral to euhedral crystals. Anhedral olivine grains are rare. Most olivine grains are <1 mm in length; a few grains are large, up to 2.3 mm in length. A few olivine grains contain chromite. Olivine grains commonly show irregular fractures. Two types of lithic inclusions are observed in olivine. The dominant type is composed mainly of Si,Al-rich glass and pyroxene with various textures (Fig. 3a). In a few melt inclusions, elongate pyroxene grains form dendritic texture and fine-grained Ti-rich phases are also present. The other type is a mafic inclusion that consists of high-Ca pyroxene, RE-merrillite, chromite, and baddeleyite (Fig. 3b). Multiple melt inclusions of the same type are observed within single olivine crystals, and different types of inclusions are also identified together in a single olivine host (Fig. 3b). These features were also observed in NWA 773 (Fagan et al. 2003).

Olivine in NWA 2977 has a limited Mg# [≡molar [Mg/(Mg + Fe)]*100], ranging from 67 to 70. The CaO contents in olivine mainly vary from 0.1 to 0.2 wt% with an average of 0.15 wt% (Table 2). However, a few grains adjacent to and within shock-induced melt veins contain higher CaO (0.31–0.88 wt%). MnO contents vary from 0.23 to 0.34 wt% and the Fe/Mn values vary from 78 to 122 with an average value of 99, which is consistent with a lunar origin. The Si,Al-rich melt inclusions contain 3.4–3.5 wt% bulk TiO_2 (Table 2).

Table 2. Compositions of major and trace elements of plagioclase, K-feldspar, olivine, the Si,Al-rich melt inclusions from Northwest Africa (NWA) 2977 and the calculated rare earth element (REE) concentrations of whole rock and mafic inclusion.

	IP35 (ol)		IP10 (pl)	IP22 (pl)	IP13 (Kfs)	26 (Kfs)	IP41 (melt)	Whole rock[a]	Mafic inclusion[b]
Major elements, wt% (electron microprobe)									
SiO_2	38.1		45.0	49.4	64.3	64.4	63.7		
TiO_2	0.08			0.11			3.38		
Al_2O_3	bd		35.2	32.3	18.5	18.8	14.1		
Cr_2O_3	0.03						0.06		
MgO	33.5		0.08	0.17	bd	0.03	2.51		
CaO	0.15		19.1	15.7	0.25	0.36	12.1		
MnO	0.24						0.05		
FeO	27.6		0.24	0.45	0.08	0.09	2.94		
Na_2O	bd		0.67	1.34	0.66	0.71	0.63		
K_2O	bd		0.09	1.24	15.4	15.3	0.27		
BaO					0.47	0.63			
Total	99.6		100.4	100.7	99.7	100.3	99.7		
Mg#	68	An	93.5	80.1	1.2	1.8			
		Ab	6.0	12.3	5.9	6.4			
		Or	0.5	7.5	91.9	90.6			
		Cs			0.9	1.1			
Trace elements, ppm (ion microprobe)									
Sc	26.8 (0.69)		1.68 (0.38)	5.38 (0.64)	1.38 (0.49)		25.8 (0.54)		
V	15.7 (0.72)		3.17 (0.15)	2.46 (0.19)	1.02 (0.08)		29.4 (0.64)		
Rb	0.71 (0.52)		0.00 (2.29)	4.77 (3.54)	714 (8.93)		9.50 (0.62)		
Sr	2.97 (0.23)		122 (1.58)	158 (2.77)	180 (2.46)		57.1 (0.97)		
Y	1.54 (0.13)		2.59 (0.13)	3.44 (0.23)	0.78 (0.04)		298 (2.19)		
Zr	1.96 (1.96)		2.08 (0.07)	0.79 (0.09)	2.37 (0.16)		357 (3.61)		
Ba	2.20 (0.24)		163 (2.63)	675 (7.48)	4507 (21.5)		146 (2.38)		
La			5.41 (0.23)	10.3 (0.62)	4.57 (0.21)		14.5 (0.61)	29.5	9347
Ce			11.0 (0.45)	16.7 (0.94)	2.00 (0.14)		41.0 (1.16)	28.5	6227
Pr			1.24 (0.06)	1.60 (0.15)	0.17 (0.02)		6.23 (0.28)	23.8	
Nd	0.02 (0.02)		4.41 (0.14)	6.34 (0.30)	0.44 (0.07)		26.9 (0.78)	21.0	2114
Sm			0.91 (0.10)	0.82 (0.13)	0.29 (0.07)		11.2 (0.56)	16.6	1388
Eu			2.13 (0.15)	3.06 (0.41)	1.02 (1.15)		0.63 (0.10)	3.3	54
Gd	0.07 (0.03)		0.46 (0.12)	0.34 (0.20)			15.1 (0.97)	13.0	1140
Tb	0.02 (0.01)		0.10 (0.02)				4.40 (0.26)	13.3	
Dy	0.19 (0.04)		0.57 (0.05)	0.64 (0.08)			35.4 (0.97)	12.9	
Ho							8.05 (0.37)	11.4	
Er	0.24 (0.04)		0.25 (0.04)	0.37 (0.07)			27.1 (0.78)	11.4	
Tm	0.05 (0.02)						4.18 (0.23)	10.8	
Yb	0.59 (0.12)			0.11 (0.05)			25.9 (1.09)	10.5	459
Lu	0.31 (0.06)						3.83 (0.28)	12.6	436

Notes: Ol = olivine; pl = plagioclase; Kfs = K-feldspar; bd = below detection limit; Numbers in brackets are errors. Errors for trace elements are 1σ standard deviation based upon counting statistics.

[a]The whole-rock REE composition of NWA 2977 was calculated based on modal abundances, densities, and the average REE concentrations of each mineral determined by secondary ion mass spectrometry.

[b]The REE composition of the mafic inclusion was calculated based on the REE concentrations of augite coupled with partition coefficients appropriate for the specific mineral composition (McKay 1989; McKay et al. 1986).

Raman spectra show that olivine adjacent to a shock-induced melt vein (Fig. 2a) has been partially transformed into its high-pressure polymorph, ringwoodite (Fig. 4). However, olivine adjacent to another melt vein (Fig. 2b) does not show a similar high-pressure phase transformation.

Pyroxene

Pyroxenes in NWA 2977 are mainly anhedral in shape. Coarse (early) pigeonite grains are usually enclosed by augite (Fig. 5a), whereas a few pigeonite grains contain patchy augite grains (Fig. 5b).

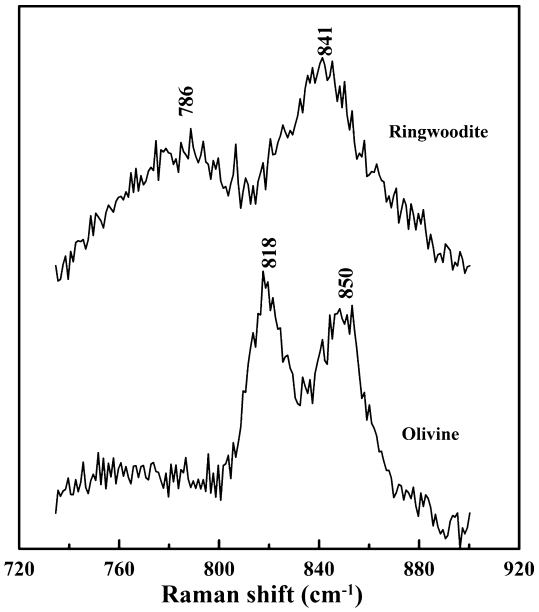

Fig. 4. Raman spectra of olivine and ringwoodite in NWA 2977.

Compositional zoning also occurs in a few pyroxene grains (Figs. 5c and 5d). Exsolution lamellae were not observed in either pigeonite or augite grains. Both low-Ca pyroxene (orthopyroxene and pigeonite) and augite also occur as late phases coexisting with phosphate minerals and baddeleyite. In this study, no high-pressure phase transformation of pyroxene was observed.

Representative chemical compositions of pyroxenes are given in Table 3. Coarse-grained (early) pigeonite shows a large variation in Wo contents from 5.6 to 20.5 (Fig. 6), with a limited variation in Mg# (70–75). Late-stage, low-Ca pyroxene ($Wo_{2.5–8.6}$) contains less Ca than early pigeonite and has Mg#s varying from 70 to 73. Augite surrounding early pigeonite has Wo contents varying from 32.7 to 37.1 and Mg#s that vary from 74 to 79. Late augite and patchy augite in early pigeonite have higher Wo contents (39.3–42.6; Fig. 6) and their Mg#s vary from 75 to 78. A few late augite grains have lower Mg#s (65–66). The augite grain in one Si,Al-rich melt inclusion of olivine has the highest Wo content (44.6) observed in this study and also contains high Al_2O_3 (4.2 wt%). The average Fe/Mn value of all pyroxenes is 51.5, consistent with a lunar origin.

Content of Al_2O_3 and TiO_2 in the pyroxenes show relatively large variations (0.56–4.2 and 0.12–1.69 wt%, respectively), and the range of Cr_2O_3 contents is 0.14–1.03 wt%. These minor elements do not show obvious correlations; however, the distribution of Ti/Al in pyroxenes (Fig. 7a) is correlated with their occurrences. Early pyroxenes usually have Ti/Al ratios < 0.25, whereas late pyroxenes have Ti/Al ratios > 0.25 (even > 0.5). A few early pyroxene grains close to shock-induced melt vein and augites in inclusions of olivine also have slightly higher Ti/Al (0.25–0.5). The Ti/(Ti + Cr) ratio of pyroxene shows a weak positive correlation with Fe/(Fe + Mg) (Fig. 7b). In detail, late-stage pyroxenes generally have higher Ti/(Ti + Cr) ratios than early pyroxenes; however, the range of Ti/(Ti + Cr) ratios in late pyroxenes is less than that in early pyroxenes.

Feldspar

Plagioclase has been transformed into maskelynite (Bunch et al. 2006) and is mainly anhedral, conforming to crystal margins of olivine and pyroxene. Most grains are several hundreds of microns in size, and a few are up to approximately 1 mm. Plagioclase does not show obvious compositional zoning on BSE images; however, a few grains show minor heterogeneity at high BSE contrast (Fig. 8a). K-feldspar (20–100 μm) mainly occurs as a late-stage interstitial (mesostasis) phase with ilmenite, phosphates, and baddeleyite, among coarse-grained olivine, pyroxene, and plagioclase. A few K-feldspar grains exhibit heterogeneity on BSE images, reflecting compositional variations (Fig. 8b).

Plagioclase is calcic ($An_{80–94}$; Table 2). Heterogeneity in the BSE images of plagioclase is correlated with variations in the An and Ab components. In a given plagioclase grain, An, Ab, and Or components vary from 80.1 to 91.9, 6.9 to 12.6, and 1.2 to 7.5, respectively. Plagioclase contains 0.21–0.63 wt% FeO. K-feldspar shows large variations in BaO contents among different grains (0.47–8.8 wt%) and within individual grains (e.g., 0.54–2.91 and 4.13–8.8 wt%). The K-feldspar grain adjacent to the Cl-rich apatite (Fig. 8a) is dominated by an orthoclase component ($Or_{90.6–91.9}$) and has low BaO contents (0.47–0.63 wt%). Most K-feldspar grains contain 0.16–0.7 wt% FeO; however, the FeO content in the K-feldspar grain (Fig. 8a) adjacent to the Cl-rich apatite is very low (0.08–0.09 wt%).

Oxide Minerals

Oxide minerals in NWA 2977 include Al,Ti-rich chromite, ilmenite, and baddeleyite. Al,Ti-rich chromite grains mainly occur along the grain boundaries between pyroxene and olivine. They are mainly equant and subhedral to euhedral in shape; a few chromite grains are anhedral, conforming to the crystal margins of adjacent olivine grains. Grain sizes of chromite vary from 10 to 400 μm. A few Al,Ti-rich chromite grains show lamellae on BSE images (Fig. 9). No chemical

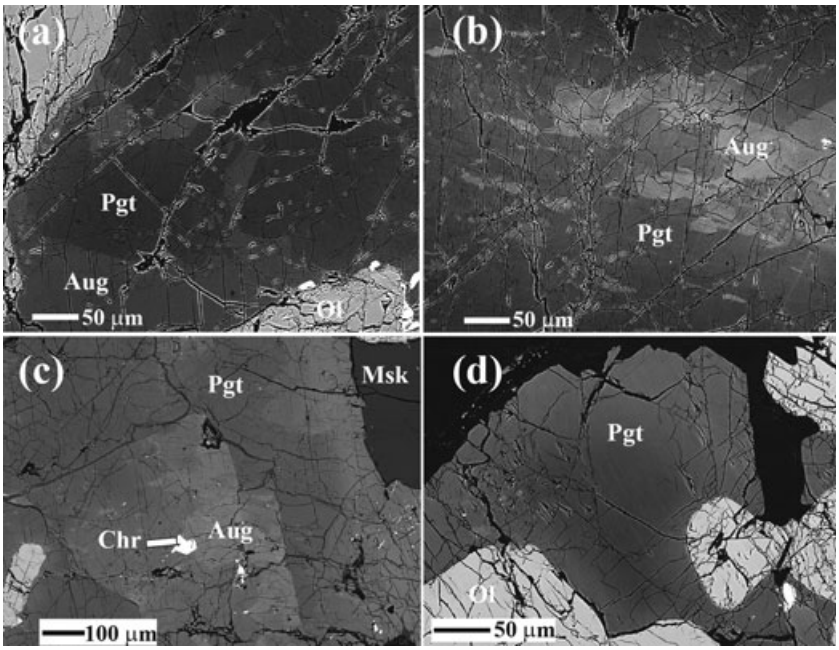

Fig. 5. Backscattered electron image of pyroxene in NWA 2977. a) Augite (Aug) enclosing coarse-grained pigeonite (Pgt). b) Pigeonite containing patchy augite. c) Pigeonite containing Al,Ti-rich chromite (Chr) with a rim of augite. d) A pigeonite with weak chemical zonation.

difference was detected between the host and the lamellae by point analysis and X-ray elemental mapping, undoubtedly due to the minute dimensions of the lamellae. However, the host and lamellae have different Raman spectra (Fig. 10). The host Al,Ti-rich chromite has two sharp peaks at 490 and 688 cm^{-1}, which can be attributed to the A_{1g} vibration in the $FeCr_2O_4$ component and the F_{2g} vibration in the Fe_2TiO_4 component (Wang et al. 2004). Besides these two peaks, a weak peak at 606 cm^{-1} is also observed. By contrast, the lamellae have four peaks at 501, 592, 644, and 690 cm^{-1}. Compared to the spectrum of the host, the lamellae have two new peaks at 592 and 644 cm^{-1}. This may suggest a different crystal structure, probably $CaTi_2O_4$-structured (cf. Chen et al. 2003). Chromite shows intergrain compositional variations ($Chr_{44–72}Spl_{15–29}Usp_{2–40}$; Table 4), with trends similar to the trend of chromites in the Apollo basalts (Fig. 11). Ilmenite is usually elongate in shape and varies from 30 to 200 μm in length; however, in a few cases, fine-grained ilmenite coexists with augite, K-feldspar, baddeleyite, and Cl-rich apatite (Fig. 8a). In one ilmenite grain, thin lamellae (< 0.5 μm in width) of chromite and rutile were observed (Fig. 12). Most ilmenite grains contain approximately 5.6 wt% MgO; however, fine-grained ilmenite grains coexisting with Cl-rich apatite have low MgO contents (~2.7 wt%; Table 4). Chromite and rutile lamellae in ilmenite are too thin for good quantitative analyses. X-ray mapping results of Ti, Fe, and Cr in ilmenite, chromite, and rutile are shown in Figs. 12b–d. Subhedral to euhedral baddeleyite mainly occurs with other late-stage phases (Fig. 13).

Phosphate Minerals

Both merrillite and apatite occur in NWA 2977 (Figs. 3b, 8, and 13). Merrillite is usually elongate, subhedral to euhedral and varies from 15 to 100 μm in size. One merrillite grain occurs in a melt inclusion in olivine (Fig. 3b). Apatite in NWA 2977 is usually anhedral to euhedral in shape and varies from 20 to 200 μm in size. Representative chemical compositions of the phosphate minerals are listed in Table 5. Most apatite grains are Cl-poor (0.03–0.35 wt% Cl) and only one apatite grain (Fig. 8a) is Cl-rich (2.49–2.70 wt% Cl).

Sulfides and Melt Veins

Sulfides are accessory phases and occur as anhedral to euhedral grains with other late-stage minerals or as mineral inclusions in chromite. Grain sizes vary from 10 to 40 μm. A few sulfide grains contain coarse exsolution lamellae. The host phase is pyrrhotite, and the lamellar phase is pentlandite. Representative compositions of sulfides are given in Table 6.

Melt veins typically contain relict mineral fragments (olivine and diopside) and show large chemical

Table 3. Compositions of major and trace elements of pyroxenes from Northwest Africa 2977.

	IP1 (aug)	IP2 (pgt)	IP16 (pgt)	IP20 (aug)	IP30 (opx)	IP36 (aug)	IP37 (pgt)	142 (aug)	27 (aug)
Major elements, wt% (electron microprobe)									
SiO_2	52.4	53.9	54.2	51.6	54.2	51.5	53.7	50.0	51.9
TiO_2	0.24	0.17	0.56	1.68	0.60	1.30	0.43	1.69	0.76
Al_2O_3	2.07	1.40	0.83	2.28	0.74	2.20	1.55	4.20	0.85
Cr_2O_3	1.01	0.73	0.19	0.37	0.30	0.48	0.34	0.19	0.17
MgO	18.5	24.3	22.7	15.4	24.0	15.1	20.6	12.7	13.5
CaO	16.3	5.87	3.37	18.6	2.09	18.9	8.10	9.85	13.0
MnO	0.18	0.28	0.31	0.22	0.29	0.20	0.32	0.20	0.25
FeO	9.21	13.9	16.7	9.26	17.9	9.23	14.5	20.5	19.3
Na_2O	0.03	bd	bd	0.05	bd	0.06	bd	0.19	0.08
Total	99.9	100.6	98.9	99.5	100.1	99.0	99.6	99.5	99.8
Mg#	78	76	71	75	71	75	72	70	65
Ti/Al	0.07	0.08	0.43	0.47	0.52	0.38	0.18	0.26	0.58
Wo	33.1	11.6	7.0	39.3	4.2	40.0	16.8	44.6	40
En	52.4	67.2	66.0	45.5	67.7	44.7	59.8	38.7	39
Fs	14.5	21.3	27.0	15.2	28.0	15.2	23.4	16.7	21
Trace elements, ppm (ion microprobe)									
Sc	5.48 (1.43)	32.5 (0.70)	34.4 (2.01)	79.3 (2.08)	39.5 (1.95)	49.2 (3.82)	41.1 (1.03)		
V	339 (3.20)	204 (1.54)	66.7 (1.88)	175 (3.40)	79.5 (1.47)	348 (3.97)	128 (1.37)		
Rb	0.70 (0.33)	0.45 (0.23)	1.90 (0.77)	1.27 (0.62)	1.18 (0.39)	1.18 (0.67)	1.59 (0.51)		
Sr	3.34 (0.26)	2.8 (0.13)	11.2 (0.47)	21.3 (1.09)	3.80 (0.18)	22.1 (0.75)	6.87 (0.34)		
Y	17.4 (0.72)	6.38 (0.24)	27.3 (1.11)	85.6 (2.39)	45.0 (1.11)	293 (3.68)	15.4 (0.48)		
Zr	12.6 (0.63)	4.11 (0.18)	116 (3.65)	120 (4.30)	66.0 (1.82)	165 (4.07)	11.7 (0.45)		
Ba	1.78 (0.20)	3.83 (0.18)	15.3 (0.79)	11.7 (1.03)	2.75 (0.13)	12.4 (0.90)	8.38 (0.52)		
La	0.49 (0.05)	0.07 (0.01)	0.72 (0.09)	3.31 (0.39)	1.28 (0.10)	50.5 (1.13)	0.27 (0.02)		
Ce	1.96 (0.15)	0.28 (0.02)	3.73 (0.29)	17.1 (1.44)	4.28 (0.25)	146 (2.88)	1.13 (0.10)		
Pr	0.55 (0.06)	0.07 (0.01)	0.56 (0.05)	3.43 (0.37)	0.82 (0.07)	21.9 (0.72)	0.22 (0.02)		
Nd	2.93 (0.15)	0.43 (0.03)	2.61 (0.17)	19.4 (1.15)	4.29 (0.16)	95.6 (1.96)	1.49 (0.08)		
Sm	1.37 (0.13)	0.19 (0.03)	1.48 (0.18)	8.08 (0.93)	2.22 (0.15)	34.7 (1.37)	0.73 (0.07)		
Eu	0.09 (0.02)		0.04 (0.03)	0.14 (0.09)	0.01 (0.02)	0.49 (0.11)	0.03 (0.01)		
Gd	2.46 (0.31)	0.53 (0.06)	2.07 (0.20)	16.7 (1.62)	4.27 (0.33)	44.8 (2.14)	1.20 (0.15)		
Tb	0.36 (0.06)	0.13 (0.02)	0.65 (0.06)	2.43 (0.26)	0.84 (0.08)	7.28 (0.44)	0.31 (0.03)		
Dy	3.50 (0.21)	1.02 (0.05)	4.39 (0.28)	13.4 (1.05)	7.14 (0.28)	52.7 (1.55)	2.59 (0.14)		
Ho	0.72 (0.09)	0.22 (0.03)	1.78 (0.18)	3.51 (0.38)	1.68 (0.11)	11.0 (0.70)	0.58 (0.05)		
Er	2.16 (0.15)	0.84 (0.04)	4.22 (0.26)	9.95 (0.72)	5.81 (0.24)	29.6 (0.92)	1.93 (0.12)		
Tm	0.37 (0.04)	0.11 (0.01)	0.95 (0.08)	0.89 (0.14)	0.91 (0.08)	3.75 (0.24)	0.29 (0.03)		
Yb	2.42 (0.22)	1.01 (0.06)	5.83 (0.39)	8.12 (0.84)	7.51 (0.37)	21.6 (1.05)	2.28 (0.18)		
Lu	0.33 (0.05)	0.17 (0.02)	1.75 (0.18)	1.00 (0.20)	1.15 (0.09)	3.18 (0.37)	0.36 (0.05)		

Notes: Aug = augite; pgt = pigeonite; opx = orthopyroxene; bd = below detection limit; Mg# = 100*Mg/(Fe + Mg). Numbers in brackets are errors. Errors for trace elements are 1σ standard deviation based upon counting statistics.

variations (e.g., MgO: 11.9–29.6 wt%; CaO: 2.8–11.7 wt%), which is a function of the local mineralogy that was melted.

Trace Element Compositions of Minerals and Melt Inclusions

The REE concentrations in olivine are low, and the CI chondrite-normalized pattern is enriched in heavy REE (HREE), with Nd = 0.04 × CI and Yb = 3.6 × CI (Fig. 14a). Sr and Ba concentrations in olivine are 2.97 and 2.20 ppm, respectively.

Pyroxene in NWA 2977 shows a large variation in REE concentrations (Fig. 14b). Low-Ca pyroxenes (two spots on orthopyroxene and six spots on pigeonite) have HREE-enriched patterns (Fig. 14b). The CI chondrite-normalized REE abundances increase gradually from La to Lu with deep negative Eu anomalies. Coarse-grained pigeonite has low REE (LREE) concentrations (La 0.3–1.1 × CI), whereas late-stage orthopyroxene and pigeonite have higher REE concentrations (La 3.1–6.6 × CI). Coarse-grained augite has a flat HREE pattern, but increasing LREE from La to Sm (Fig. 14b). The REE concentrations (La 2.1 × CI)

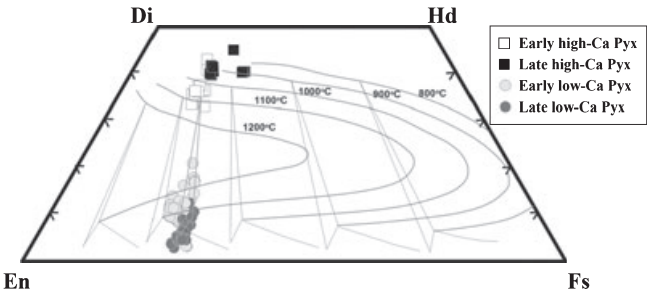

Fig. 6. Compositional variation of pyroxene in NWA 2977. The quadrilateral isotherms of pyroxene (Pyx) are from Sack and Ghiorso (1994).

of IP1 augite are distinctly higher than those of coexisting pigeonite. Late-stage augite has higher REE concentrations (La ~14–16 × CI), and shows increasing LREE from La (~14–16 × CI) to Sm (~55–58 × CI), but decreasing HREE concentrations from Gd (47–85 × CI) to Lu (23–41 × CI). The augite inclusion in olivine shown in Fig. 3b has the highest REE concentrations (La 215 × CI) and an essentially flat LREE pattern. All augite grains show deep negative Eu anomalies. Sr and Ba concentrations in pyroxene vary from 2.8 to 22.1 ppm and from 1.8 to 22.1 ppm, respectively. The Sr concentration has a positive correlation with Ba.

Plagioclase has LREE-enriched patterns with positive Eu anomalies (Fig. 14c). No obvious relationship between REE concentrations and Ab contents was observed in this study. The REE patterns for K-feldspar grains have a steeply decreasing slope from La (~20–76 × CI) to Nd (~1 × CI), and then a steeply increasing slope from Nd to Eu (~18–124 × CI). HREE concentrations in K-feldspar grains are below detection limits.

Both merrillite and apatite show LREE-enriched patterns with deep negative Eu anomalies (Fig. 14d). Merrillite contains high REE concentrations (La 16,865–50,696 × CI), typical of most basalt merrillites. Two of three spots on merrillite (IP7 and IP15) have almost identical REE patterns and abundances. However, IP29 merrillite has a steeper decreasing slope from La (50,696 × CI) to Lu (1412 × CI). Apatite has lower REE concentrations (La 560–6090 × CI) than merrillite and show large variations in REE patterns and abundances (Fig. 14d). The Cl-rich apatite has higher REE concentrations (La 4754 × CI) than Cl-poor apatite grains (La 560 × CI and 1195 × CI, respectively). The IP27 apatite shows higher REE concentrations and a steeper HREE slope than IP9 apatite. The REE pattern of apatite IP27 is similar to that of neighboring merrillite (IP29), although concentrations are distinctly lower.

Two Si,Al-rich melt inclusions in olivine (IP41 and IP42 in Table 2) have similar REE concentrations (La 62–81 × CI) and patterns. The HREE concentrations are slightly higher than LREE, but the patterns are essentially flat with small negative Eu anomalies (Fig. 14a).

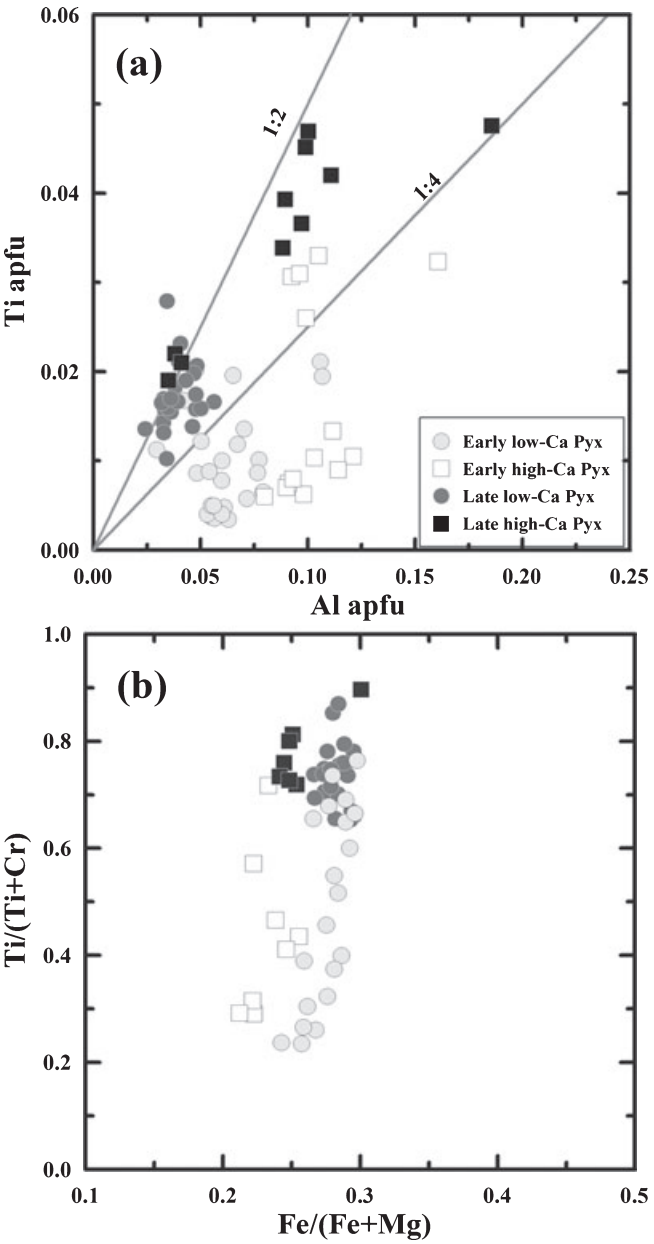

Fig. 7. Compositional variations of pyroxene (Pyx) in NWA 2977. a) Ti versus Al in atoms per 6 oxygen formula units (apfu). b) Molar Ti/(Ti + Cr) versus molar Fe/(Fe + Mg).

Pb/Pb Age of Baddeleyite

Fifteen ion microprobe analyses were performed on 12 baddeleyite grains in NWA 2977. Thirteen data points were used for $^{207}Pb/^{206}Pb$ dating calculations, and two other data points were excluded because the

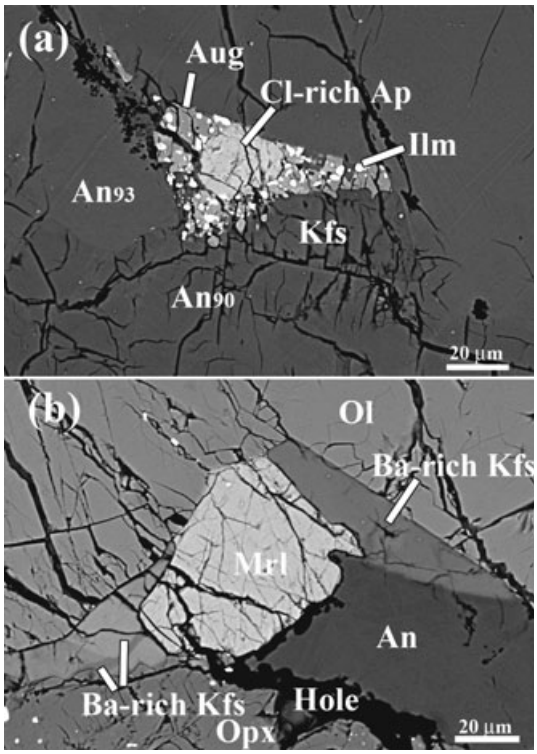

Fig. 8. Backscattered electron images of feldspar and phosphates in NWA 2977. a) A mesostasis region composed of augite (Aug), ilmenite (Ilm), Cl-rich apatite (Ap) occurring in the interstices among anorthite (An) and K-feldspar (Kfs). b) Anorthite occurring with merrillite (Mrl) and Ba-rich K-feldspar (Ba-rich Kfs) in the interstices among olivine (Ol) and orthopyroxene (Opx). The Ba-rich K-feldspar grain in the lower left shows chemical heterogeneity.

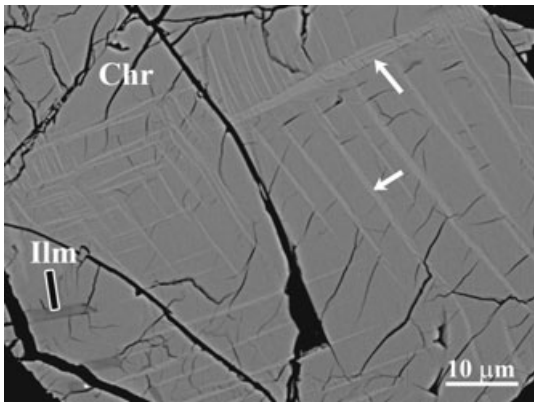

Fig. 9. Backscattered electron image of an Al,Ti-rich chromite (Chr) grain with two sets of lamellae (indicated by white arrows), possibly representing a high-pressure polymorph. Ilmenite (Ilm) lamellae also occur in this Al,Ti-rich chromite grain.

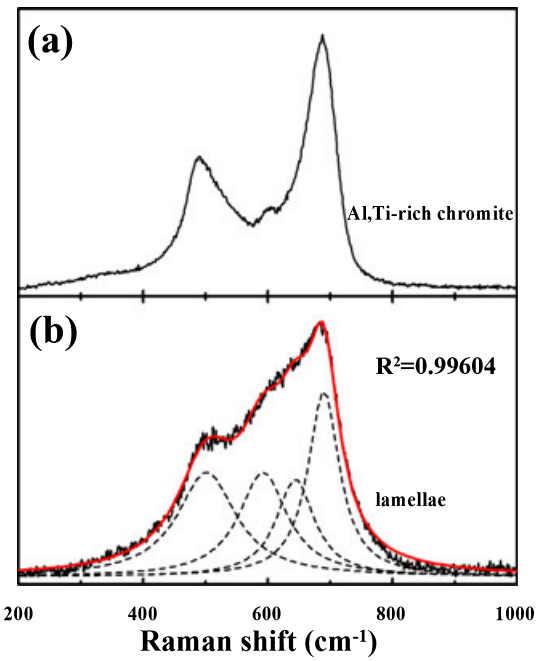

Fig. 10. Raman spectra of chromite (a) and lamellae (b) in NWA 2977. The dashed lines in (b) are the subspectra used to fit the whole spectrum (red line).

measurements were partially on cracks near baddeleyite and phosphate minerals. All analyses gave almost identical results within errors (Table 7) and yield a weighted mean $^{207}Pb/^{206}Pb$ age of 3123 ± 7 (2σ) Ma.

DISCUSSION

Terrestrial Contamination in NWA 2977

Meteorites found in hot and cold desert environments can be altered in their chemistry due to oxidation and interaction with terrestrial water during their extensive residence on Earth (e.g., Floss and Crozaz 1991; Crozaz and Wadhwa 2001; Crozaz et al. 2003; Jolliff et al. 2003; Korotev et al. 2003, 2009; Hsu et al. 2004). Crozaz and Wadhwa (2001) and Crozaz et al. (2003) documented several geochemical features within constituent minerals that can be attributed to terrestrial contamination in meteorites from hot deserts. The features include: (1) enrichments of the LREE, (2) enrichments of Sr and Ba, and (3) Ce anomalies in olivine and pyroxene (Crozaz and Wadhwa 2001; Crozaz et al. 2003). In addition, calcite veins are a characteristic feature of terrestrial alteration, and these may be observed throughout the whole meteorite (e.g., Jolliff et al. 2003). Terrestrial weathering can also cause alteration of Fe-Ni metal and sulfide in meteorites.

The presence of calcite deposits on the surface of the meteorite (Fig. 13) and in the form of fracture fillings (Fig. 2a) indicates that terrestrial weathering is

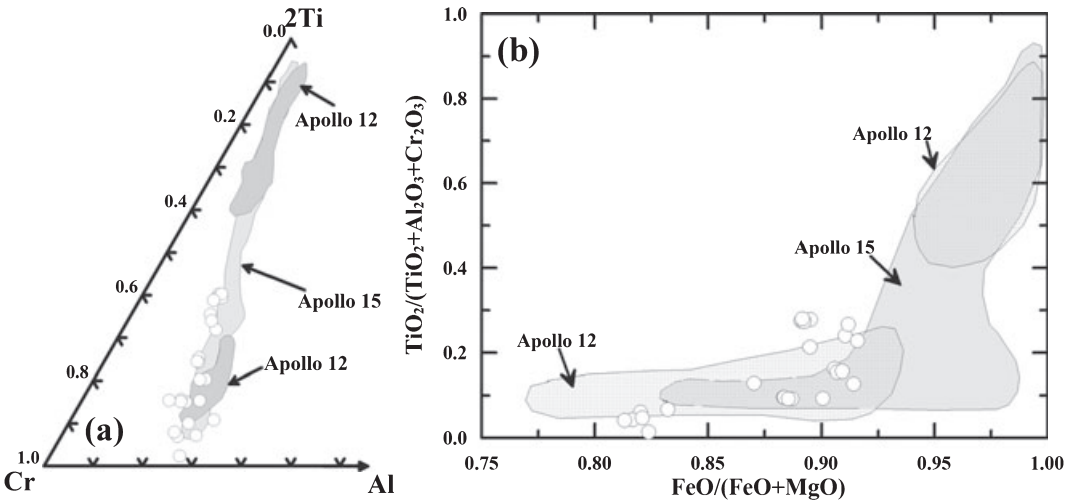

Fig. 11. Chemical variations of chromite in NWA 2977 in the (a) Cr-2Ti-Al ternary and in the diagram of (b) FeO/(FeO + MgO) versus $TiO_2/(TiO_2 + Al_2O_3 + Cr_2O_3)$ in wt%, compared with chromite-ulvöspinel from Apollo 12 and 15 samples (Anand et al. 2003).

Table 4. Major-element compositions of chromite and ilmenite in Northwest Africa 2977.

	Chromite				Ilmenite					
Major elements, wt% (electron microprobe)										
SiO_2	0.09	0.19	0.29	0.10	0.37	0.08	0.23	0.11	0.08	0.95
TiO_2	7.96	15.1	5.85	12.6	5.79	2.86	0.93	9.73	55.0	50.7
Al_2O_3	11.3	8.03	11.6	9.56	10.5	13.8	13.2	9.23	0.04	0.09
Cr_2O_3	42.4	32.2	43.9	36.8	46.5	49.4	53.1	40.8	0.35	0.47
MgO	4.85	4.65	4.27	4.32	4.11	6.13	5.70	3.78	5.60	2.74
FeO	32.6	38.5	32.4	36.8	32.3	27.3	26.6	36.3	38.2	41.7
MnO	0.32	0.37	0.30	0.36	0.29	0.32	0.29	0.37	0.46	0.43
CaO									0.04	1.16
Total	99.5	99.0	98.6	100.5	99.9	99.9	100.1	100.3	99.8	98.2
Spl	22.6	16.4	23.9	19.0	21.3	27.3	26.4	18.8		
Chr	57.0	44.2	60.7	49.1	63.6	65.5	71.2	55.9		
Usp	20.3	39.4	15.4	31.9	15.1	7.2	2.4	25.3		

Note: Spl = spinel; Chr = chromite; Usp = ulvöspinel.

present in NWA 2977. Jolliff et al. (2003) suggested that correlated variations of Sr and Ba in pyroxene and olivine in NWA 773 could be the result of terrestrial contamination. If this is correct, then pyroxene and olivine in NWA 2977 may be affected by terrestrial alteration, because Sr and Ba in these minerals are also correlated. However, there are a few clues arguing against severe alteration effects on the REE distributions in NWA 2977 minerals. First, we did not observe any weathering of Fe-Ni metal and sulfide grains in NWA 2977. Second, the olivine and pyroxene grains studied do not show any enrichments of the LREE. Third, most pyroxene grains show no Ce anomalies. Thus, although the NWA 2977 meteorite has experienced some degree of terrestrial contamination, this did not significantly disturb the REE distributions in its constituent minerals.

Records of Shock Metamorphism in NWA 2977

Shock metamorphism is critical to understanding the thermal histories of meteorites because investigations have shown that isotopic systems used for chronology can be disturbed by shock metamorphism (e.g., Ar/Ar system: Cohen et al. 2000; U-Pb system: Zhang et al. 2010b). In NWA 2977, there are some mineralogical records of shock metamorphism. Plagioclase has been transformed into maskelynite. The occurrence of maskelynite indicates a shock stage of up to S5, corresponding a pressure about 45–55 GPa and a postshock temperature of at least 600 °C, based on the criteria for ordinary chondrites of Stöffler et al. (1991). A few thin melt veins and melt pockets with relict mineral fragments are present in NWA 2977; however, no high-pressure mineral phases were observed in these melt veins

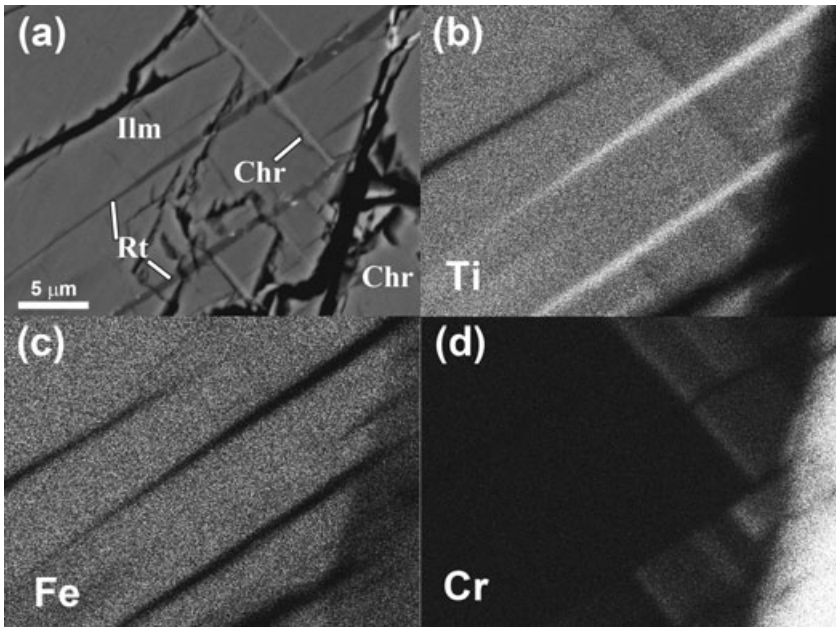

Fig. 12. Array of a backscattered electron image (a) and Ti (b), Fe (c), and Cr (d) X-ray maps of ilmenite (Ilm) and lamellae of chromite (Chr) and rutile (Rt).

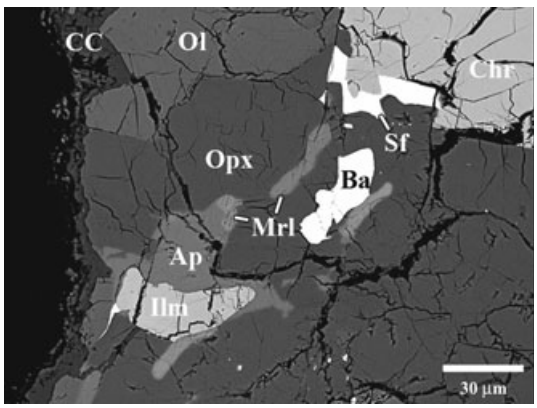

Fig. 13. Backscattered electron image of a representative area in NWA 2977 containing late-stage minerals: ilmenite (Ilm), orthopyroxene (Opx), merrillite (Mrl), apatite (Ap), sulfide (Sf), and baddeleyite (Ba). Ol, olivine; Chr, chromite; CC, calcium calcite.

and melt pockets. This suggests that NWA 2977 experienced shock metamorphism of at least S3. Some olivine adjacent to a melt vein has been partially transformed into ringwoodite. The occurrence of ringwoodite implies that NWA 2977 could have experienced local shock up to stage S6 (Stöffler et al. 1991). Al,Ti-rich chromite contains exsolution lamellae that may be a high-pressure polymorph of Al,Ti-rich chromite. Based on static high-pressure experimental results, Chen et al. (2003) estimated the *P–T* conditions of the transformation from pure chromite to $CaTi_2O_4$-structured polymorph are 20–23 GPa and 1800–2000 °C. The presence of this high-pressure phase indicates that NWA 2977 was extensively shocked, although the exact *P–T* conditions of the transformation from Al,Ti-rich chromite to its high-pressure polymorph are difficult to estimate, because Al,Ti-rich chromite has a significantly different chemical composition than pure chromite. In summary, the pressure distribution in NWA 2977 during shock metamorphism was heterogeneous, with evidence for shock stages of S3–S6. At the same time, because maskelynite did not transform back to plagioclase, the cooling rate of NWA 2977 following shock metamorphism must have been rapid, but the kinetics for this are unknown at present.

Crystallization Sequence of NWA 2977

The high abundance of olivine in NWA 2977 and its rounded to euhedral shape indicate that olivine is the first phase to crystallize. A few chromite grains may also have simultaneously crystallized with olivine because of their occurrence as inclusions in olivine. Pyroxene crystallized after olivine because most pyroxene grains are anhedral and enclose olivine grains. Early pyroxene crystallized prior to plagioclase, which occurs only as an interstitial and anhedral phase. However, during or following the crystallization of plagioclase, late pyroxene crystallized together with ilmenite, K-feldspar, phosphate minerals, and baddeleyite from the residual melt. Sulfides also formed very late because they mainly occur together with

Table 5. Compositions of major and trace elements of phosphates from Northwest Africa 2977.

	IP7 (mrl)	IP29 (mrl)	IP9 (ap)	IP14 (ap)	IP27 (ap)	IP32 (ap)
Major elements, wt% (electron microprobe)						
P_2O_5	43.7	42.1	41.4	40.1	40.6	40.3
SiO_2	0.19	0.28	0.56	0.03	0.57	0.19
MgO	3.44	3.27	0.10	0.15	0.18	0.15
CaO	45.0	39.5	53.8	56.5	53.8	54.7
FeO	0.93	0.72	0.48	0.6	0.47	0.59
Na_2O	0.55	0.05	0.12	0.03	0.04	
F	0.61	0.51	1.98	2.81	3.14	2.84
Cl	0.01	0.00	2.49	0.2	0.17	0.25
Total	94.2	86.1	94.1	98.7	97.3	97.2
Trace elements, ppm (ion microprobe)						
La	3958 (28)	11,898 (64)	1116 (17)	131 (6)	1429 (14)	280 (11)
Ce	10,060 (50)	28,085 (109)	2653 (29)	368 (11)	3695 (25)	860 (22)
Pr	1242 (15)	3228 (32)	274 (8)	49 (2)	442 (7)	104 (7)
Nd	5575 (41)	13,525 (84)	1180 (22)	190 (6)	1778 (19)	538 (15)
Sm	1360 (31)	2353 (52)	261 (15)	48 (4)	339 (12)	174 (9)
Eu	18 (3)	18 (3)	8 (2)	1.6 (0.3)	5 (1)	5 (1)
Gd	1284 (36)	1814 (66)	238 (17)	51 (5)	306 (16)	147 (14)
Tb	231 (9)	281 (16)	52 (4)	12 (1)	62 (4)	35 (4)
Dy	1523 (23)	1447 (33)	307 (10)	51 (3)	250 (8)	185 (8)
Ho	321 (9)	274 (12)	79 (4)	12 (1)	46 (3)	41 (4)
Er	818 (17)	655 (22)	212 (8)	27 (2)	104 (4)	108 (5)
Tm	101 (5)	73 (5)	27 (2)	3.7 (0.4)	11 (1)	17 (2)
Yb	607 (18)	380 (23)	185 (8)	20 (2)	48 (4)	106 (6)
Lu	82 (7)	34 (7)	27 (3)	2.4 (0.4)		15 (2)

Notes: Mrl = merrillite; ap = apatite. Numbers in brackets are errors. Errors for trace elements are 1σ standard deviation based upon counting statistics.

Table 6. Representative compositions of sulfides in Northwest Africa 2977.

	Pyrrhotite				Pentlandite					
Major elements, wt% (electron microprobe)										
S	36.3	36.7	36.7	36.7	36.4	33.3	33.6	33.0	33.4	34.3
Fe	62.1	62.2	62.2	62.2	62.1	36.6	38.0	35.7	35.9	41.2
Ni	0.07	0.06	bd	0.03	0.06	26.4	25.0	27.4	28.8	20.4
Cr	0.30	0.04	bd	0.04	bd	0.45	0.78	bd	0.08	bd
Co	bd	bd	bd	bd	bd	2.57	2.88	3.22	1.25	2.37
Si	0.04	0.03	0.03	0.03	0.06	0.03	0.03	0.03	0.04	0.07
Total	98.8	99.0	99.0	99.0	98.7	99.4	100	99.4	99.5	98.3

Note: bd = below detection limit.

late-stage phases, although a few grains are included in pyroxene.

Previous investigations of pyroxenes in lunar basalts (e.g., Bence et al. 1970, 1971; Bence and Papike 1972; Fagan et al. 2002, 2003; Arai et al. 2010) suggested that the Ti/Al ratios of pyroxene are closely correlated with the crystallization order of pyroxene and plagioclase. When pyroxene precipitates prior to plagioclase, Ti/Al ratios are close to 0.25, which is attributed to subequal proportions of two cation substitutions $Ti + 2Al \rightarrow Mg + 2Si$ and $2Al \rightarrow Mg + Si$. When pyroxene cocrystallizes with plagioclase, the substitution $Ti + 2Al \rightarrow Mg + 2Si$ is dominant, and as a consequence, Ti/Al ratios of the pyroxenes would be close to 0.5. In the case of NWA 2977 (Fig. 7a), most early pyroxenes have Ti/Al ratios close to or lower than 0.25. However, late pyroxenes have Ti/Al values higher than 0.25 and close to 0.5. This supports the conclusion from petrographic observations that early pyroxenes crystallized prior to plagioclase, whereas late pyroxenes either cocrystallized with, or crystallized after, plagioclase.

It is well known that REE partition coefficients are distinctly higher in high-Ca pyroxene than in low-Ca pyroxenes (e.g., McKay 1989). In NWA 2977, a few low-Ca pyroxenes (e.g., IP16) have higher REE concentrations than coarse-grained augite (e.g., IP1). In

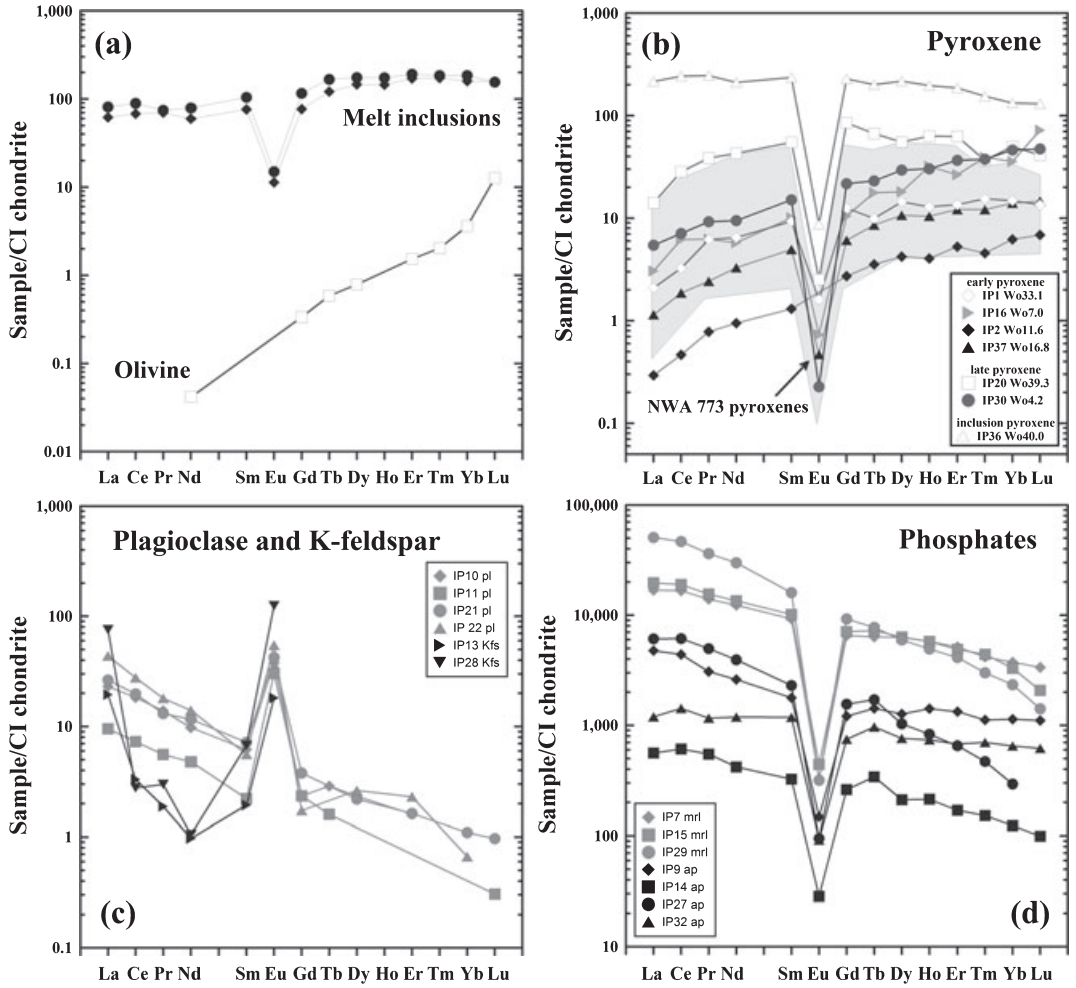

Fig. 14. CI chondrite-normalized REE patterns of minerals and Si,Al,Ca-rich melt inclusions in NWA 2977. a) Olivine shows a typical HREE-enriched pattern. The Si,Al-rich melt inclusions show almost flat LREE and HREE; however, HREE concentrations are slightly higher than LREE. b) Pyroxene in NWA 2977 shows a large variation of REE concentrations. The highest REE concentrations are in augite from the mafic inclusion in olivine. Mesostasis augite has higher REE concentrations than pigeonite. However, one coarse augite grain (IP1) has lower REE concentrations than mesostasis low-Ca pyroxene. Shaded area in (b) is from Jolliff et al. (2003). c) Anorthite and K-feldspar in NWA 2977 have LREE-enriched patterns with positive Eu anomalies. d) Merrillite has higher REE concentrations than apatite.

addition, REE concentrations of early pigeonite are distinctly lower than those of late-stage low-Ca pyroxenes, and REE concentrations of late augite are distinctly higher than those of early augite, the normal situation with such lunar pyroxenes. These features are a direct function of fractional crystallization. Because the REEs are incompatible in olivine and pyroxene, crystallization of these phases results in enrichment of the REEs in late-stage melts. In summary, petrographic observations, Ti/Al ratios, and REE geochemistry show that early pyroxenes with low Ti/Al ratios (<0.25) and LREE concentrations crystallized during and after the crystallization of olivine and before the onset of plagioclase crystallization. Late-stage pyroxenes, which have higher Ti/Al ratios (>0.25) and higher REE concentrations, formed during and after the crystallization of plagioclase. This is in agreement with previous investigations on NWA 773 (Fagan et al. 2003; Jolliff et al. 2003).

The fine-grained mineral assemblage shown in Fig. 8a probably represents the final crystallization product of residual melt, the mesostasis. Two lines of evidence provide support for this. First, the apatite in this assemblage has a higher Cl concentration than other apatite grains that are F-dominant. Fluorine is preferentially incorporated into apatite over Cl, and the F/Cl ratio in a melt will decrease with progressive crystallization of apatite (Stormer and Carmichael 1971; Jolliff et al. 1993). In NWA 2977, merrillite cocrystallized with apatite, indicating that, although apatite is stable,

Table 7. Northwest Africa (NWA) 2977 baddeleyite Pb/Pb data determined by multicollector secondary ion mass spectrometry.

	$(^{204}Pb/^{206}Pb)_m$	±1σ (%)	$(^{207}Pb/^{206}Pb)_m$	±1σ (%)	$(^{207}Pb/^{206}Pb)_c$	±1σ (%)	$t_{207/206}$ (Ma)	±2σ (%)
nwa@1	9.17E-06	57.3	0.2430	0.37	0.2429	0.71	3139	24
nwa@2	4.91E-04	9.0	0.2453	0.47	0.2400	0.72	3120	24
nwa@3	1.19E-04	14.5	0.2404	0.39	0.2391	0.71	3114	24
nwa@4	1.75E-03	7.3	0.2609	0.65	0.2421	1.07	3134	35
nwa@5	9.62E-05	21.5	0.2419	0.49	0.2409	0.71	3126	24
nwa@6	2.04E-04	12.5	0.2428	0.45	0.2406	0.71	3124	24
nwa@7	5.57E-04	8.5	0.2465	0.46	0.2405	0.71	3123	24
nwa@8	7.95E-04	10.6	0.2468	0.69	0.2382	0.96	3108	31
nwa@9	0.00E + 00	100.0	0.2417	0.35	0.2417	0.71	3131	24
nwa@10	2.66E-03	4.7	0.2702	0.52	0.2415	0.99	3130	32
nwa@11	5.98E-04	8.9	0.2447	0.50	0.2382	0.76	3108	25
nwa@12	1.92E-04	13.2	0.2418	0.46	0.2397	0.71	3118	24
nwa@13	3.69E-03	5.5	0.2802	0.73	0.2404	1.46	3122	47

Notes: The values of $(^{204}Pb/^{206}Pb)_m$ and $(^{207}Pb/^{206}Pb)_m$ are the measured value; the error is the in-run analytical error. The value of $(^{207}Pb/^{206}Pb)_c$ is the calculated value after common ^{204}Pb correction; the error includes propagation of common Pb correction and external uncertainty of the Phalaborwa baddeleyite standard.

the concentrations of F and Cl in the melt are not very high, otherwise merrillite would be not stable. Assuming relatively low concentrations of F and Cl in the melt, crystallization of fluorapatite would consume most of the F in the melt and cause local Cl enrichment. The Cl-rich apatite shown in the fine-grained mineral assemblage of Fig. 8a must have crystallized after most other phosphate, in a region of local Cl enrichment, and represents the final crystallization product of the residual melt. Second, ilmenite in this fine-grained mineral assemblage contains lower MgO (2.7 wt%) than most ilmenite (~5.5 wt%), whereas augite in this assemblage has a lower Mg# (65–66) than other augite (74–79). Papike et al. (1991, 1998) noted that ilmenite compositions correlate with the bulk composition of the rock and reflect magmatic chemistry. Ilmenites with the highest Mg contents tend to come from relatively high-Mg rocks (Papike et al. 1991, 1998). The low Mg abundance of ilmenite in this mineral assemblage might reflect a local low MgO content in the residual melt of NWA 2977, after crystallization of abundant Mg-rich minerals (olivine and pyroxene). Similarly, the Mg# of augite in the assemblage is the lowest among all of the ferromagnesian silicates in NWA 2977. These features also provide evidence that the fine-grained mineral assemblage represents a late-stage crystallization product.

In lunar rocks, chromite and rutile usually occur together with Fe metal, as a result of the reduction of Cr-bearing ilmenite: Cr-bearing ilmenite + O_2 (g) → chromite + rutile + Fe metal (El Goresy 1976). In this study, one ilmenite grain (Fig. 9) was observed containing lamellar chromite and rutile; however no Fe-metal grains were observed. One possibility is that Fe-metal grains did form according to the proposed reaction, but that due to their relatively high mobility, Fe-metal grains migrated along mineral boundaries and were not observed. An alternative possibility is that the formation of chromite and rutile lamellae in ilmenite was not related to the above reduction reaction. Naslund (1987) argued that the simultaneous exsolution of spinel and baddeleyite (which has a same crystal structure as rutile) could develop in an ilmenite host without oxidation or reduction if the ratio of spinel:baddeleyite were approximately 3:1. Because rutile has a crystal structure similar to baddeleyite, this interpretation is probably reasonable for NWA 2977, although it is difficult to estimate the proportions of chromite and rutile.

REE Abundance of the Whole Rock and Origin of Melt Inclusions in Olivine

We calculated the whole-rock REE composition of NWA 2977 based on modal abundances and densities of minerals and their average REE concentrations (Fig. 15). Also shown in Fig. 15 is the REE pattern of KREEP rock (Warren 1988), and the measured whole-rock REE concentrations of the olivine-gabbro portion in NWA 773 (Jolliff et al. 2003). The result shows that whole-rock REE concentrations and patterns are mainly controlled by merrillite, although its modal abundance is low. The calculated whole-rock REE composition is similar to the measured whole-rock REE composition of the olivine-gabbro portion in NWA 773 (Fig. 15), especially in LREE (Jolliff et al. 2003). The calculated whole-rock REE pattern of NWA 2977 is parallel to

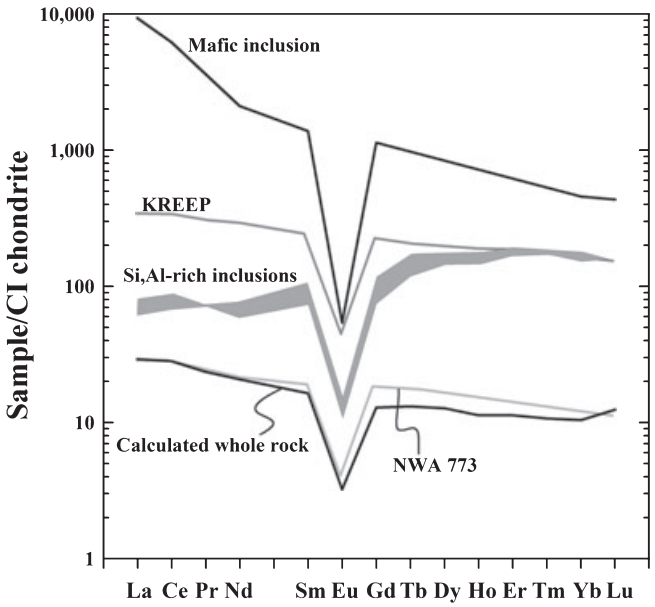

Fig. 15. CI chondrite-normalized REE pattern of the calculated whole-rock composition of NWA 2977, compared with the REE patterns of KREEP (Warren 1988) and the measured whole-rock composition of the olivine-gabbro portion in NWA 773 (Jolliff et al. 2003). The measured REE patterns of the Si,Al-rich melt inclusions and the calculated REE pattern of the mafic inclusion in olivine are also shown. The whole-rock REE composition of NWA 2977 was calculated using modal abundances, densities, and the average REE concentrations of each mineral determined by SIMS. The REE composition of the mafic inclusion was calculated using the REE concentrations of augite coupled with partition coefficients appropriate for the specific mineral composition (McKay et al. 1986; McKay 1989).

that of KREEP rock (Fig. 15). This KREEP-like REE pattern may be due to addition of a KREEP component or could be caused by low-degree partial melting (e.g., Borg et al. 2009). However, the negative initial ε_{Nd} value of NWA 2977 reported by Nyquist et al. (2009) suggests that NWA 2977 probably originated from a KREEP-rich source. Therefore, the KREEP-like REE pattern of NWA 2977 is likely due to the addition of KREEP component rather than small degrees of partial melting. The parental magma of NWA 2977 might have obtained its KREEP-like REE features in the magma chamber deep in the mantle or during ascent of the magma.

In NWA 2977, the Si,Al-rich melt inclusions show an enrichment of the HREE over the LREE (Fig. 14a). Because the minerals in these Si,Al-rich melt inclusions are very fine-grained, the REE pattern measured reflects the original chemical features of the inclusions. By contrast, the minerals in the mafic inclusion are relatively coarse-grained, implying that major elements in the inclusion have equilibrated with the host olivine or possibly even with the melt around the host olivine. However, because REEs have low diffusion coefficients in olivine and, therefore, would not equilibrate easily with the melt surrounding the olivine grains (Gaetani and Watson 2000), we argue that the REE compositions of the melt inclusions in olivine can be used to estimate the geochemical features of their parental melts, even if the major elements (e.g., Mg and Fe) have completely equilibrated. We calculated the REE composition of the mafic inclusion using the measured REE concentrations of the augite and partitioning coefficients between augite and melt, assuming that the melt inclusion represents a closed system for REEs and that all minerals equilibrated with the melt. The calculated result shows that the mafic inclusion has extremely high REE concentrations and a LREE-enriched pattern (Fig. 15). The two kinds of inclusions distinctly differ in abundances and REE patterns from each other and are also different from that of the whole rock (Fig. 15).

There are several ways to interpret the coexistence of two distinctly different inclusions in olivine. One possibility is that the two inclusion types represent immiscible silicate liquids during the early stages of igneous differentiation of the parental melt of NWA 2977, as Fagan et al. (2003) proposed to explain andesitic and silica-rich melt inclusions in olivine. However, this interpretation seems unlikely because of the distinct difference in grain sizes in the two different inclusions. Furthermore, compared to late-stage interstitial augite grains, the extremely high REE concentrations of augite in the mafic inclusion in olivine are also difficult to explain by the silicate liquid immiscibility. Another possibility is that the two types of inclusions formed at different stages. The mafic inclusion could represent a relict fragment from a country rock captured during the ascent of the parental magma of NWA 2977. If this is the case, the mafic inclusion could represent a fragment of the KREEPy component present in NWA 2977. At the same time, if we assume that the parental magma of NWA 2977 has a LREE-enriched pattern similar to that of the calculated whole rock, crystallization of olivine and pyroxene would result in more enrichment of the LREE in the melt, in contrast to the HREE-enriched pattern of the Si,Al-rich inclusions. One possibility for interpreting this HREE-enriched pattern is that the Si,Al-rich melt inclusions represent a less-evolved melt parental to NWA 2977. In summary, the mafic inclusion could represent a fragment of a KREEP-rich rock captured during the ascent of the NWA 2977 parental melt, whereas the Si,Al-rich inclusions could reflect the features of a less-evolved melt parental to NWA 2977.

Crystallization Age of NWA 2977

Northwest Africa 2977 has been dated by a series of isotopic methods including the Pb-Pb dating method used in this study. Ages between 3.10 ± 0.05 and 3.29 ± 0.11 Ga were obtained by whole-rock and mineral isochron Sm-Nd, Rb-Sr methods (Nyquist et al. 2009), and the baddeleyite $^{207}Pb/^{206}Pb$ method (this study). By contrast, the ^{40}Ar-^{39}Ar dating technique gave an age of 2.77 ± 0.04 Ga (Burgess et al. 2007). Considering the high-intensity shock metamorphism (up to S6) experienced by NWA 2977, the ^{40}Ar-^{39}Ar age probably reflects the time of a secondary thermal event after crystallization of the rock that caused some radiogenic ^{40}Ar loss. On the other hand, the consistency between the Sm-Nd, Rb-Sr ages and the baddeleyite $^{207}Pb/^{206}Pb$ age suggests that these ages reflect the crystallization age of NWA 2977. Overall, the ages determined for NWA 2977 are similar to those of the olivine-gabbro portion of NWA 773 (Fernandes et al. 2003; Burgess et al. 2007; Borg et al. 2009). Combined with similar petrologic and geochemical features (e.g., Fagan et al. 2003; Jolliff et al. 2003; Zeigler et al. 2007), the chronological similarity suggests that NWA 2977 is paired with the olivine-gabbro portion of NWA 773.

Acknowledgments—The authors would like to express their gratitude to Michael Farmer for providing the sample, to Jianyun Tan for preparing the section, to Allan D. Patchen for his kind assistance during EMP analysis at the University of Tennessee, to Yu Liu and Guoqiang Tang for baddeleyite Pb/Pb dating, and to Dr. Yanjun Guo and Junying Ding for acquiring Raman spectra of minerals. This manuscript benefited from critical and helpful comments from three referees (Drs. Kentaro Terada, Tim Fagan, and Amy Gaffney) and associate editor Dr. Randy Korotev. The study was supported by NSFC Grants 40703015 and 41703052 (Z. A. C.) and 40773046 (H. W. B.), and the Planetary Geosciences Institute at the University of Tennessee, through a NASA Cosmochemistry Program, NNG05GG03G (L. A. T.).

Editorial Handling—Dr. Randy Korotev

REFERENCES

Alexander C. M. O'D. 1994. Trace element distributions within ordinary chondrite chondrules: Implications for chondrule formation conditions and precursors. *Geochimica et Cosmochimica Acta* 58:3451–3467.

Anand M., Taylor L. A., Misra K. C., Demidova S. I., and Nazarov M. A. 2003. KREEPy lunar meteorite Dhofar 287A: A new lunar mare basalt. *Meteoritics & Planetary Science* 38:485–499.

Anders E. and Grevesse N. 1989. Abundances of the elements—Meteoritic and solar. *Geochimica et Cosmochimica Acta* 53:197–214.

Arai T., Hawke B. R., Giguere T. A., Misawa K., Miyamoto M., and Kojima H. 2010. Antarctic lunar meteorites Yamato-793169, Asuka-881757, MIL 05035, and MET 01210 (YAMM): Launch pairing and possible cryptomare origin. *Geochimica et Cosmochimica Acta* 74:2231–2248.

Bence A. E. and Papike J. J. 1972. Pyroxenes as recorders of lunar basalt petrogenesis: Chemical trends due to crystal-liquid interaction. Proceedings, 3rd Lunar Science Conference. pp. 431–469.

Bence A. E., Papike J. J., and Prewitt C. T. 1970. Apollo 12 clinopyroxenes: Chemical trends. *Earth and Planetary Science Letters* 8:393–399.

Bence A. E., Papike J. J., and Lindsley D. H. 1971. Crystallization histories of clinopyroxenes in two porphyritic rocks from Oceanus Procellarum. *Proceedings, 2nd Lunar Science Conference*. pp. 559–574.

Borg L. E., Gaffney A. M., Shearer C. K., DePaolo D. J., Hutcheon I. D., Owens T. L., Ramon E., and Brennecka G. 2009. Mechanisms for incompatible-element enrichment on the Moon deduced from the lunar basaltic meteorite Northwest Africa 032. *Geochimica et Cosmochimica Acta* 73:3963–3980.

Bunch T. E., Wittke J. H., Korotev R. L., and Irving A. J. 2006. Lunar meteorite NWA 2700, NWA 2727, and NWA 2977: Mare basalt/gabbro breccias with affinities to NWA 773 (abstract #1375). 37th Lunar and Planetary Science Conference. CD-ROM.

Burgess R., Fernandes V. A., Irving A. J., and Bunch T. E. 2007. Ar-Ar ages of NWA 2977 and NWA 3160—Lunar meteorite paired with NWA 773 (abstract #1603). 38th Lunar and Planetary Science Conference. CD-ROM.

Chen M., Shu J. F., Xie X. D., and Mao H. K. 2003. Natural $CaTi_2O_4$-structured $FeCr_2O_4$ polymorph in the Suizhou meteorite and its significance in mantle mineralogy. *Geochimica et Cosmochimica Acta* 67:3937–3942.

Cohen B. A., Swindle T. D., and Kring D. A. 2000. Support for the lunar cataclysm hypothesis from lunar meteorite impact melt ages. *Science* 290:1754–1756.

Crozaz G. and Wadhwa M. 2001. The terrestrial alteration of Saharan Shergottites Dar al Gani 476 and 489: A case study of weathering in a hot desert environment. *Geochimica et Cosmochimica Acta* 65:971–978.

Crozaz G., Floss C., and Wadhwa M. 2003. Chemical alteration and REE mobilization in meteorites from hot and cold deserts. *Geochimica et Cosmochimica Acta* 67:4727–4741.

El Goresy A. 1976. Oxide minerals in lunar rocks. In *Oxide minerals*, edited by Rumble D. Reviews in Mineralogy, vol. 5. Washington, D.C.: Mineralogical Society of America. pp. EG1–EG46.

Fagan T. J., Taylor G. J., Keil K., Bunch T. E., Wittke J. H., Korotev R. L., Jolliff B. L., Gillis J. J., Haskin L. A., Jarosewich E., Clayton R. N., Mayeda T. K., Fernandes V. A., Burgess R., Turner G., Eugster O., and Lorenzetti S. 2002. Northwest Africa 032: Product of lunar volcanism. *Meteoritics & Planetary Science* 37:371–394.

Fagan T. J., Taylor G. J., Keil K., Hicks T. L., Killgore M., Bunch T. E., Wittke J. H., Mittlefehldt D. W., Clayton R. N., Mayeda T. K., Eugster O., Lorenzetti S., and Norman M. D. 2003. Northwest Africa 773: Lunar origin and iron-enrichment trend. *Meteoritics & Planetary Science* 38:529–554.

Fernandes V. A., Burgess R., and Turner G. 2003. ^{40}Ar-^{39}Ar chronology of lunar meteorites Northwest Africa 032 and 773. *Meteoritics & Planetary Science* 38:555–564.

Floss C. 2000. Complexities on the acapulcoite-lodranite parent body: Evidence from trace element distributions in silicate minerals. *Meteoritics & Planetary Science* 35:1073–1085.

Floss C. and Crozaz G. 1991. Ce anomalies in the LEW 85300 eucrite: Evidence for REE mobilization during Antarctic weathering. *Earth and Planetary Science Letters* 107:13–24.

Floss C. and Jolliff B. 1998. Rare earth element sensitivity factors in calcic plagioclase (anorthite). In *Secondary ion mass spectrometry, SIMS XI*, edited by Gillen G., Lareau R., Bennett J., and Stevie F. New York, New York, USA: John Wiley & Sons. pp. 785–788.

Floss C., James O. B., McGee J. J., and Crozaz G. 1998. Lunar ferroan anorthosite petrogenesis: Clues from trace element distributions in FAN subgroups. *Geochimica et Cosmochimica Acta* 62:1255–1283.

Floss C., Crozaz G., Jolliff B., Benedix G., and Colton S. 2008. Evolution of the winonaite parent body: Clues from silicate mineral trace element distributions. *Meteoritics & Planetary Science* 43:657–674.

Gaetani G. A. and Watson E. B. 2000. Open system behavior of olivine-hosted melt inclusions. *Earth and Planetary Science Letters* 183:27–41.

Heaman L. M. 2009. The application of U–Pb geochronology to mafic, ultramafic and alkaline rocks: An evaluation of three mineral standards. *Chemical Geology* 261:43–52.

Hsu W. 1995. Ion microprobe studies of the petrogenesis of enstatite chondrites and eucrites. Ph.D. thesis, Washington University, St. Louis, Missouri, USA. 380 pp.

Hsu W. B., Guan Y., Wang H. N., Leshin L. A., Wang R. C., Zhang W. L., Chen X. M., Zhang F. S., and Lin C. Y. 2004. The lherzolitic shergottite Grove Mountains 99027: Rare earth element geochemistry. *Meteoritics & Planetary Science* 39:701–709.

Hsu W. B., Zhang A., Bartoschewitz R., Guan Y. B., Ushikubo T., Krähenbühl U., Niedergesaess R., Pepelnik R., Reus U., Kurtz T., and Kurtz P. 2008. Petrography, mineralogy, and geochemistry of lunar meteorite Sayh al Uhaymir 300. *Meteoritics & Planetary Science* 43:1363–1381.

Jolliff B. L., Haskin L. A., Colson R. O., and Wadhwa M. 1993. Partitioning in REE-saturating minerals: Theory, experiment, and modelling of whitlockite, apatite, and evolution of lunar residual magmas. *Geochimica et Cosmochimica Acta* 57:4069–4094.

Jolliff B. L., Korotev R. L., Zeigler R. A., and Floss C. 2003. Northwest Africa 773: Lunar mare breccias with a shallow-formed olivine-cumulate component, inferred very-low-Ti (VLT) heritage, and a KREEP connection. *Geochimica et Cosmochimica Acta* 67:4857–4879.

Jolliff B. L., Wieczorek M. A., Shearer C. K., and Neal C. R., editors. 2006. In *New views of the Moon*. In Reviews in Mineralogy and Geochemistry, vol. 60. Washington, D.C.: Mineralogical Society of America, p. 721.

Jolliff B. L., Zeigler R. A., and Korotev R. L. 2007. Compositional characteristics and petrogenetic relationsips among the NWA 773 clan of lunar meteorites (abstract #1489). 38th Lunar and Planetary Science Conference. CD-ROM.

Korotev R. L. 2005. Lunar geochemistry as told by lunar meteorites. *Chemie der Erde—Geochemistry* 65:297–346.

Korotev R. L., Jolliff B. L., Zeigler R. A., Gillis J. J., and Haskin L. A. 2003. Feldspathic lunar meteorites and their implications for compositional remote sensing of the lunar surface and the composition of the lunar crust. *Geochimica et Cosmochimica Acta* 67:4895–4923.

Korotev R. L., Zeigler R. A., Jolliff B. L., Irving A. J., and Bunch T. E. 2009. Compositional and lithological diversity among brecciated lunar meteorites of intermediate iron composition. *Meteoritics & Planetary Science* 44:1287–1322.

Li X. H., Liu Y., Li Q. L., Guo C. H., and Chamberlain K. R. 2009. Precise determination of Phanerozoic zircon Pb/Pb age by multicollector SIMS without external standardization. *Geochemistry Geophysics Geosystems* 10:Q04010, doi:10.1029/2009GC002400.

Li Q. L., Li X. H., Liu Y., Tang G. Q., Yang J. H., and Zhu W. G. 2010. Precise U-Pb and Pb-Pb dating of Phanerozoic baddeleyite by SIMs with oxygen flooding technique. *Journal of Analytical Atomic Spectroscopy* 25:1107–1113.

McKay G. A. 1989. Partitioning of rare earth elements between major silicate minerals and basaltic melts. In *Geochemistry and mineralogy of rare earth elements*, edited by Lipin B. R. and McKay G. A. Reviews in Mineralogy vol. 21, pp. 45–77.

McKay G., Wagstaff J., and Yang S.-R. 1986. Clinopyroxene REE distribution coefficients for shergottites: The REE content of the Shergotty melt. *Geochimica et Cosmochimica Acta* 50:927–937.

Naslund H. R. 1987. Lamellae of baddeleyite and Fe-Cr-spinel in ilmenite. *Canadian Mineralogist* 25:91–96.

Nemchin A. A., Pidgeon R. T., Healy D., Grange M. L., Whitehouse M. J., and Vaughan J. 2009. The comparative behavior of apatite-zircon U-Pb systems in Apollo 14 breccias: Implications for the thermal history of the Fra Mauro Formation. *Meteoritics & Planetary Science* 44: 1717–1734.

Niihara T., Kaiden H., Misawa K., and Sekine T. 2009. U-Pb isotopic systematic of experimentally shocked baddeleyite (abstract #1562). 40th Lunar and Planetary Science Conference. CD-ROM.

Nyquist L. E., Shih C. Y., Reese Y. D., and Irving A. J. 2009. Sm-Nd and Rb-Sr ages and isotopic systematic for NWA 2977, a young basalt from the PKT. *Meteoritics & Planetary Science* 44:A159–A159.

Papike J., Taylor L., and Simon S. 1991. Lunar minerals. In *Lunar sourcebook: A user's guide to the Moon*, edited by Heiken G. H., Vaniman D. T., and French B. M. Cambridge University Press, Cambridge, UK, pp. 121–181.

Papike J. J., Ryder G., and Shearer C. K. 1998. Lunar samples. In *Planetary materials*, edited by Papike J. J. Reviews in Mineralogy and Geochemistry vol. 36. Washington, D.C.: Mineralogical Society of America. pp. 5.1–5.234.

Rasmussen B., Fletcher I. R., and Muhling J. R. 2008. Pb/Pb geochronology, petrography and chemistry of Zr-rich accessory minerals (zirconolite, tranquillityite and baddeleyite) in mare basalt 10047. *Geochimica et Cosmochimica Acta* 72:5799–5818.

Sack R. O. and Ghiorso M. S. 1994. Thermodynamics of multicomponent pyroxenes: II. Phase relations in the quadrilateral. *Contributions to Mineralogy and Petrology* 116:287–300.

Stöffler D., Keil K., and Scott E. R. D. 1991. Shock metamorphism of ordinary chondrites. *Geochimica et Cosmochimica Acta* 55:3854–3867.

Stormer J. C. and Carmichael L. S. E. 1971. Fluorine-hydroxyl exchange in apatite and biotite: A potential igneous geothermometer. *Contributions to Mineralogy and Petrology* 31:121–131.

Takeda H., Yamaguchi A., Bogard D. D., Karouji Y., Ebihara M., Ohtake M., Saiki K., and Arai T. 2006. Magnesian anorthosites and a deep crustal rock from the farside crust of the moon. *Earth and Planetary Science Letters* 247:171–184.

Terada K., Anand M., Sokol A. K., Bischoff A., and Sano Y. 2007. Cryptomare magmatism 4.35 Gyr ago recorded in lunar meteorite Kalahari 009. *Nature* 450:849–852.

Wang A., Kuebler K. E., Jolliff B. L., and Haskin L. A. 2004. Raman spectroscopy of Fe-Ti-Cr-oxides, case study: Martian meteorite EETA79001. *American Mineralogist* 89:665–680.

Warren P. H. 1985. The magma ocean concept and lunar evolution. *Annual Review of Earth and Planetary Science* 13:201–240.

Warren P. H. 1988. KREEP: Major-element diversity, trace-element uniformity (almost). In *Workshop on Moon in transition: Apollo 14, KREEP and evolved lunar rocks*, edited by Taylor G. J. and Warren P. H. LPI Technical Report 89-03. Houston, Texas: Lunar and Planetary Institute. pp. 106–110.

Warren P. H. and Kallemeyn G. W. 1991. Geochemical investigation of five lunar meteorites: Implications for the composition, origin and evolution of the lunar crust. *Proceedings of the NIPR Symposium on Antarctic Meteorites* 4:91–117.

Zeigler R. A., Korotev R. L., and Jolliff B. L. 2007. Petrography, geochemistry, and pairing relationships of basaltic lunar meteorite stones NWA 773, NWA 2700, NWA 2727, NWA 2977, and NWA 3160 (abstract #2109). 38th Lunar and Planetary Science Conference. CD-ROM.

Zhang A. C. and Hsu W. B. 2008. Mineralogical and Raman spectroscopic studies of Northwestern Africa 2977 lunar meteorite. *Meteoritics & Planetary Science* 43:A176–A176.

Zhang A. C., Hsu W. B., Wang R. C., and Ding M. W. 2006. Pyroxene polymorphs in melt veins of the heavily shocked Sixiangkou L6 chondrite. *European Journal of Mineralogy* 18:719–726.

Zhang A. C., Taylor L. A., Hsu W. B., Floss C., Li X. H., and Liu Y. 2010a. Petrogenesis of lunar meteorite Northwestern Africa 2977: Rare earth element geochemistry and baddeleyite Pb/Pb dating (abstract #1052). 41st Lunar and Planetary Science Conference. CD-ROM.

Zhang A. C., Hsu W. B., Li Q. L., Liu Y., Jiang Y., and Tang G. Q. 2010b. SIMS Pb/Pb dating of Zr-rich minerals in lunar meteorites Miller Range 05035 and LaPaz Icefield 02224: Implications for the petrogenesis of mare basalt. *Science China Earth Sciences* 53:327–334.

Zinner E. and Crozaz G. 1986. Ion probe determination of the abundances of all the rare earth elements in single mineral grains. In *Secondary ion mass spectrometry, SIMS V*, edited by Benninghoven A., Colton R. J., Simons D. S., and Werner H. W. New York: Springer-Verlag. pp. 444–446.